gels

MDPI

Article

Study on Space Charge Behavior and Insulation Performance of Copper Phthalocyanine-Regulated Silicone Gels

Chao Xiao [1], Kangheng Chen [2] and Yalin Wang [2,*]

[1] State Key Laboratory of Advanced Power Transmission Technology, China Electric Power Research Institute Co., Ltd., Beijing 100192, China; xchao2003@163.com
[2] School of Electrical Engineering, Shanghai Jiao Tong University, Shanghai 200240, China; nefarious@sjtu.edu.cn
* Correspondence: wangyalin2014@sjtu.edu.cn

Abstract

With the development of high-voltage direct-current (HVDC) transmission and high-power-density power electronic equipment, space charge accumulation in silicone gels under direct-current (DC) or unipolar square-wave electric fields, together with the resulting local electric-field distortion, has become an important factor affecting insulation reliability. To improve the insulation performance of silicone gel, silicone gels with different copper (β-type) phthalocyanine (CuPc) contents were prepared. The effects of CuPc doping on space charge, trap characteristics, and insulation performance were investigated by the pulsed electroacoustic (PEA) method, depolarization-current measurements, and DC breakdown tests. The results show that CuPc can significantly suppress space charge accumulation, with CuPc-0.5 exhibiting the strongest suppression. After 1800 s of short circuit, the residual bulk charge densities of both CuPc composites decrease to below 1 C/m^3, whereas that of silicone gel remains approximately 2.5 C/m^3. The effective trap energy distributions reconstructed from isothermal relaxation current (IRC) measurements reveal an increase in the effective deep-trap density after CuPc incorporation. Furthermore, the reconstructed internal electric-field distributions demonstrate that CuPc addition substantially mitigates space-charge-induced electric-field distortion. The partial-discharge inception voltage (PDIV) under square-wave voltage of CuPc addition is slightly higher than that of silicone gel. CuPc significantly improves DC breakdown performance: compared with silicone gel, the characteristic DC breakdown strengths of CuPc-0.5 and CuPc-1 increase by approximately 23.1% and 13.0%, respectively. CuPc affects space charge accumulation and DC insulation performance by regulating localized states and the trapping, detrapping, and migration processes of charge carriers.

Keywords: silicone gels; copper phthalocyanine; space charge; trap; packaging insulation

Check for updates

Academic Editors: Sung-Hyuk Sunwoo and Filippo Rossi

Received: 13 October 2026
Revised: 5 November 2026
Accepted: 11 November 2026
Published: 17 November 2026

Copyright: © 2026 by the authors. Licensee MDPI, Basel, Switzerland. This article is an open access article distributed under the terms and conditions of the Creative Commons Attribution (CC BY) license.

1. Introduction

Silicone gel has excellent electrical insulation properties, heat resistance, elasticity, and environmental adaptability and is widely used in high-voltage insulation, cable accessories, and the encapsulation of power electronic devices [1–5]. With the development of HVDC transmission and high-voltage, high-power-density power electronic equipment, insulating materials are subjected to increasingly severe electrical and thermal stresses during long-term operation, imposing higher requirements on the long-term insulation reliability of silicone gel. Under a DC or unipolar square-wave electric field, charge carriers can be injected from the electrodes into the polymer, migrate under the action of the electric field,

and be trapped by localized states within the material, thereby leading to space charge accumulation. Previous studies have shown that long-term service, material aging, and different electric-field conditions can significantly alter the space-charge and charge-decay characteristics of silicone gel [6–9]. The additional electric field generated by space charge further modifies the original electric-field distribution inside the material. Local field enhancement may promote charge injection and transport and ultimately affect the aging and breakdown characteristics of the material. Therefore, regulating carrier transport and space charge behavior in silicone gel is an important approach to improving its DC insulation performance.

The space charge behavior of silicone gel is closely related to the trap states within the material. Trap energy levels and trap density can affect carrier trapping, detrapping, and migration processes, thereby further determining charge accumulation and dissipation [10,11]. In recent years, introducing functional fillers into silicone gel or polydimethylsiloxane (PDMS) to regulate polymer/filler interfaces, trap structures, and carrier-transport characteristics has become an important approach to improving electrical performance. Zhang et al. found that the introduction of nano-SiO_2 can significantly alter space charge accumulation in PDMS and further affect its DC breakdown performance; under complex environments such as humid-heat conditions, SiO_2 doping can likewise regulate charge accumulation and the internal electric-field distribution [12]. A series of studies by Du et al. on SiC/silicone gel composites showed that SiC fillers can significantly change the nonlinear conductivity, carrier migration, and space charge characteristics of the material, while factors such as crystal form, particle distribution, and temperature further influence the charge-transport process [13–16]. In addition, Al_2O_3 surface modification, ZnO microvaristor fillers, and other nanoparticles have also been used to regulate the surface charge, conductivity, and local electric-field distribution of silicone gel [17,18].

Unlike conventional inorganic insulating fillers such as SiO_2 and Al_2O_3, CuPc is an organic semiconductor with a planar macrocyclic π-conjugated structure, and its molecular electronic structure exhibits distinct charge-trapping and charge-transport characteristics [19]. Previous studies have introduced CuPc into silicon-containing polymers and PDMS systems and found that CuPc can significantly alter the dielectric response of the material; its dispersion state and intermolecular interactions have important effects on the electrical properties of the composites [20]. Studies of charge transport in CuPc itself further indicate that carrier migration is strongly affected by localized states and traps and may exhibit multiple trapping-and-release characteristics. Therefore, after CuPc is incorporated into silicone gel, it may not only modify the original trap structure through the polymer/filler interface, but its own conjugated electronic states may also participate directly in the carrier-transport process.

At present, research on CuPc/polymer composites is mainly focused on high-dielectric materials, flexible actuation, and organic electronic devices [21–23], whereas relatively few studies have addressed the relationships among space charge, trap states, and breakdown performance of CuPc-doped silicone gel under high DC electric fields. In particular, how variations in CuPc content affect carrier trapping–detrapping processes, bulk space charge accumulation, and the resulting internal electric-field distortion has not yet been systematically investigated.

Therefore, silicone gel specimens with different CuPc contents were prepared in this study. The PEA method was used to investigate the evolution of space charge within the materials under stepwise DC voltages and during short circuit, while polarization/depolarization currents were used to analyze charge relaxation and trap characteristics. Space charge accumulation and the resulting internal electric-field distortion were further analyzed, and DC breakdown experiments were conducted to investigate the effect of CuPc

doping on macroscopic insulation performance. On this basis, the relationships among CuPc content, trap states, carrier transport, space charge, and DC breakdown performance were analyzed to clarify the mechanism by which CuPc regulates the insulation performance of silicone gel.

2. Results and Discussion

To systematically analyze the effects of CuPc doping on the charge-transport behavior and insulation performance of silicone gel, samples with different CuPc contents were comparatively investigated in terms of space charge distribution, depolarization current and trap characteristics, partial discharge, and DC breakdown performance. Three types of specimens were investigated and designated as silicone gel, CuPc-0.5, and CuPc-1, corresponding to CuPc contents of 0, 0.5, and 1 wt.%, respectively, relative to the total mass of the specimens.

2.1. Effect of CuPc Doping on Space Charge Behavior

During polarization, the applied DC electric field establishes electrode-induced charges and may lead to charge injection and accumulation within the specimen. After the voltage is removed and the electrodes are short-circuited, the subsequent evolution of the charge profiles reflects the redistribution and dissipation of residual charge.

The measured space charge distributions were visualized as two-dimensional heat maps using Origin software, as shown in Figure 1. The horizontal and vertical axes represent the measurement time and position along the specimen thickness, respectively. The color scale indicates the polarity and magnitude of the space charge density, with red and yellow representing positive charges, blue representing negative charges, and green indicating regions with approximately zero charge density. The two horizontal dashed lines indicate the anode and cathode, while the vertical dashed lines denote the switching times of the applied electric fields of 3, 5, 8, 10, and 15 kV/mm. The first four stages each lasted 600 s, and the final stage lasted 1800 s. The electrodes were then short-circuited for 1800 s.

As the applied voltage increases stepwise, the charge peaks at the electrode/sample interfaces of all three samples gradually increase, indicating that the enhanced electric field promotes charge formation near the electrodes. Compared with the induced charge at the electrode interfaces, the changes in charge distribution within the bulk of the samples are of greater interest. Silicone gel exhibits relatively pronounced bulk space charge accumulation at higher applied voltages. In particular, during the 15 kV/mm stage, the charge region near one electrode gradually extends into the sample, forming a relatively broad space charge distribution region. After removal of the applied voltage, appreciable residual charge remains inside the sample, indicating that some carriers enter the material during long-term DC polarization and are trapped by localized states, preventing their immediate dissipation after short circuit.

After the addition of CuPc, the space charge distribution inside the samples changes markedly. In CuPc-0.5, charge is mainly concentrated near the electrodes, with substantially reduced penetration into the interior of the material, and the residual bulk charge after short circuit is also significantly lower than that in silicone gel. CuPc-1 likewise exhibits suppression of space charge accumulation; however, a certain range of charge distribution still remains inside the sample, and the degree of suppression is weaker than that in CuPc-0.5. These results indicate that CuPc addition can modify charge injection and transport in silicone gel under a DC electric field, but this effect does not continue to increase with increasing CuPc content.

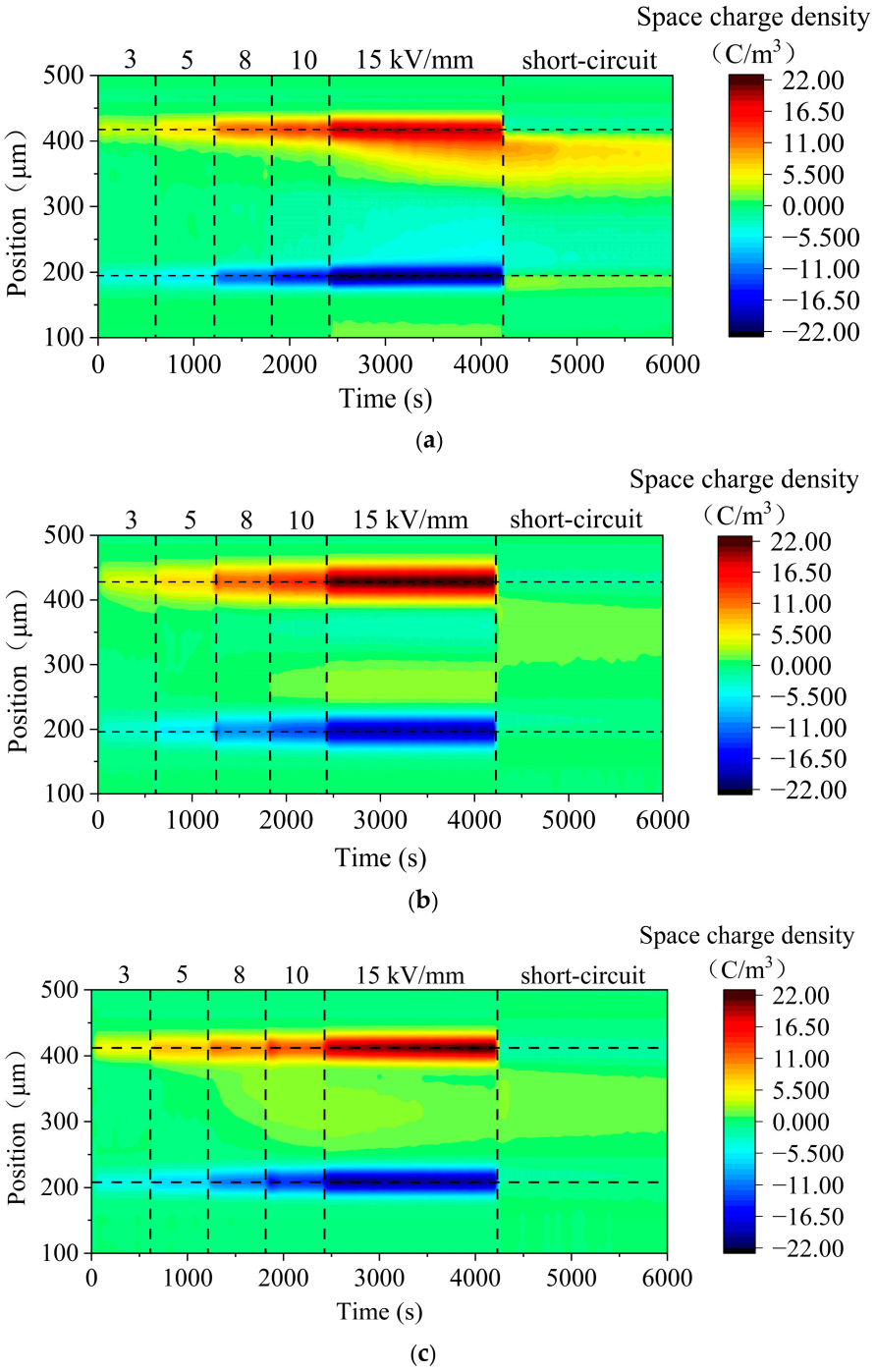


Figure 1. Spatial and temporal distribution of space charge: (**a**) silicone gel; (**b**) CuPc-0.5; (**c**) CuPc-1.

To quantitatively evaluate the bulk space charge accumulation, the mean absolute bulk space charge density was calculated as follows:

$$\rho(t) = \frac{1}{x_2 - x_1}\int_{x_1}^{x_2}|\rho(x,t)|dx \quad (1)$$

where x denotes the position coordinate along the specimen thickness; x_1 and x_2 represent the positions of the lower and upper electrodes (cathode and anode), respectively; and $\rho(x, t)$ is the space charge density at position x at time t after short-circuiting.

The mean absolute space charge density during the short-circuit stage further verifies the above results. As shown in Figure 2, the mean absolute bulk space charge density of all three samples gradually decreases with short-circuit time. Throughout the short-circuit

process, silicone gel consistently exhibits the highest mean absolute space charge density, whereas CuPc-0.5 exhibits the lowest. At the beginning of the short circuit, the mean absolute space charge density of silicone gel is approximately 3.6 C/m^3, whereas those of CuPc-0.5 and CuPc-1 are only approximately 1.1 and 1.3 C/m^3, respectively. After 1800 s of short circuit, approximately 2.5 C/m^3 of space charge remains in silicone gel, whereas the values for both CuPc-0.5 and CuPc-1 decrease to below 1 C/m^3. This demonstrates that CuPc addition significantly reduces residual space charge in the material after long-term DC polarization, with CuPc-0.5 showing the most pronounced suppression.

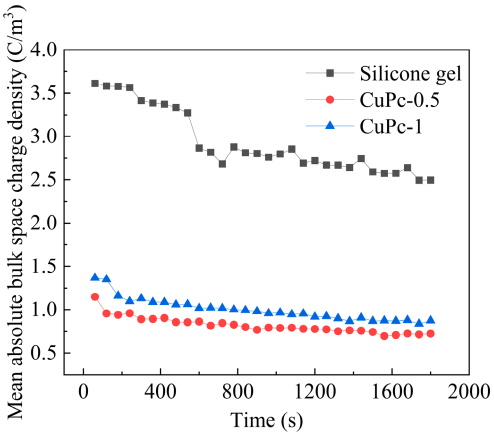


Figure 2. Mean absolute bulk space charge density in short circuit after 15 kV/mm application.

The space charge results during voltage application and short circuit show that the introduction of CuPc significantly alters carrier injection and migration in silicone gel. The relatively high bulk space charge formed in silicone gel indicates that some carriers can enter the material from the electrodes and continuously migrate inward. The significantly reduced bulk space charge in CuPc-0.5 indicates that the localized electronic states introduced by CuPc and the CuPc/silicone gel interfaces can alter carrier-transport pathways and restrict long-range migration into the material. In contrast, the suppression of space charge is somewhat weaker in CuPc-1, indicating that the charge-transport mechanism changes further as the CuPc content increases. Therefore, the regulation of space charge by CuPc does not increase monotonically with CuPc content but instead exhibits a clear concentration dependence. The effects of CuPc on charge transport are analyzed further below in conjunction with the depolarization-current and trap-characteristic results.

2.2. IRC and Trap Characteristics

The PEA and isothermal relaxation current (IRC) measurements provide complementary information on charge relaxation during short-circuit depolarization. The PEA method resolves the spatial distribution of residual charge within the specimen, as quantified in Figure 2, whereas IRC measurements record the external short-circuit current associated with charge transport and polarization relaxation after voltage removal, as shown in Figure 3. The fitted curves were reconstructed from the effective occupied-trap energy distributions obtained using the inversion method described in Section 4.4. The two measurements characterize different aspects of the depolarization process. The two signals were acquired in alternating time windows rather than simultaneously. Therefore, the PEA profiles and IRC curves represent complementary measurements under the same polarization–depolarization protocol.

The IRC decay curves of silicone gel, CuPc-0.5, and CuPc-1 during short-circuit depolarization are shown in Figure 3. The IRCs of all three materials gradually decay as the

short-circuit time increases, but clear differences are observed among the samples. Silicone gel exhibits the lowest IRC, approximately 10 pA at the beginning of the short circuit, followed by relatively slow variation. The initial IRC of CuPc-0.5 is approximately 37 pA, whereas that of CuPc-1 further increases to approximately 110 pA, markedly higher than those of the other two samples.

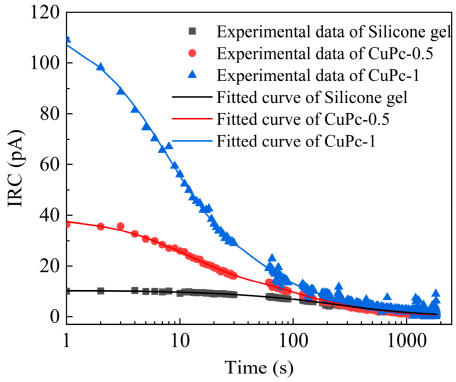


Figure 3. IRC measured curves and fitting curves during short circuit at 20 °C.

The IRC measurements show that CuPc incorporation significantly enhances the relaxation-current response after voltage removal, with CuPc-1 exhibiting the highest initial current. The measured IRC may include contributions from trapped-carrier release and transport, as well as dipolar and interfacial polarization relaxation. Notably, although the CuPc-containing composites exhibit higher IRC responses than silicone gel, their bulk space charge densities measured by PEA are substantially lower. This difference reflects the distinct physical quantities characterized by the two methods: IRC records the external current associated with charge relaxation, whereas PEA characterizes the spatial distribution of accumulated charge.

The effective trap energy distributions reconstructed from the IRC measurements are shown in Figure 4. Compared with silicone gel, both CuPc-0.5 and CuPc-1 exhibit higher effective trap densities in the deep-energy region of the analyzed spectrum, indicating an increased contribution from deep trapping states after CuPc incorporation. Deep traps can restrict long-range carrier migration by capturing charge carriers and increasing their residence times in localized states. This interpretation is consistent with the PEA results, which show reduced charge penetration and lower bulk space charge densities in both CuPc-containing composites. Therefore, the combined IRC and PEA results indicate that CuPc modifies the trap-related electrical response and suppresses bulk space charge accumulation. The relationship between trapping characteristics and charge transport is discussed further in Section 2.5.1.

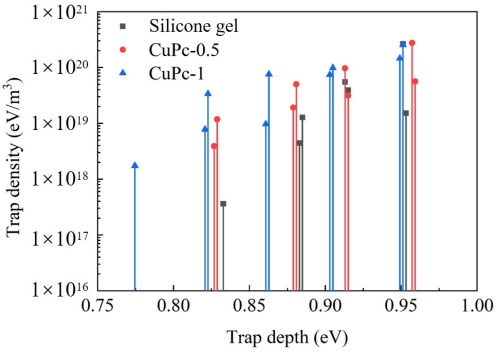


Figure 4. Trap energy density distribution.

2.3. Effect of CuPc Doping on PDIV

Figure 5 compares the PDIV measured under an identical rod–plane electrode configuration and unipolar square-wave excitation. The PDIVs (peak value of positive square-wave voltage) of the CuPc-0.5 and CuPc-1 samples are generally slightly higher than the PDIV of silicone gel. The pu PDIVs of silicone gel, CuPc-0.5, and CuPc-1 are approximately 3.18, 3.34, and 3.26 kV, respectively. The mean PDIVs of CuPc-0.5 and CuPc-1 are approximately 5.0% and 2.5% higher than that of silicone gel, respectively. Therefore, under the present test conditions, CuPc doping has a slight positive effect on the PDIV of silicone gel.

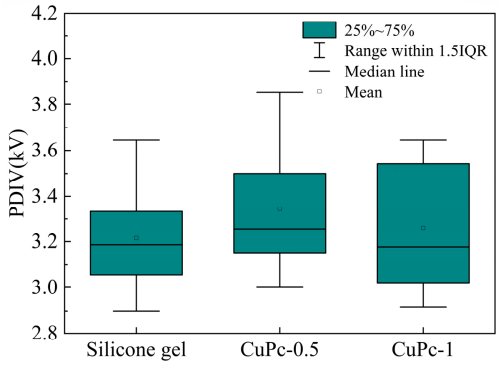


Figure 5. Statistical distribution of PDIV.

2.4. Effect of CuPc Doping on DC Breakdown Performance

As shown in Figure 6, the DC breakdown data were analyzed using a two-parameter Weibull distribution. The characteristic breakdown strengths E_0 of silicone gel, CuPc-0.5, and CuPc-1 are 66, 81, and 74 kV/mm, respectively, as shown in Table 1. Compared with silicone gel, the characteristic breakdown strengths of CuPc-0.5 and CuPc-1 increase by approximately 23.1% and 13.0%, respectively. Thus, CuPc-0.5 exhibits the highest DC breakdown strength among the three samples. The Weibull shape parameters β are 10, 26, and 23 for silicone gel, CuPc-0.5, and CuPc-1, respectively. The higher β values of the CuPc-containing samples indicate a narrower dispersion of breakdown data and improved consistency of the breakdown performance. Notably, this trend is opposite to that of the residual space charge density after short circuit: CuPc-0.5 has the lowest residual space charge, followed by CuPc-1, while silicone gel has the highest. This indicates a relatively clear correspondence between the degree of residual-space charge suppression and DC breakdown performance.

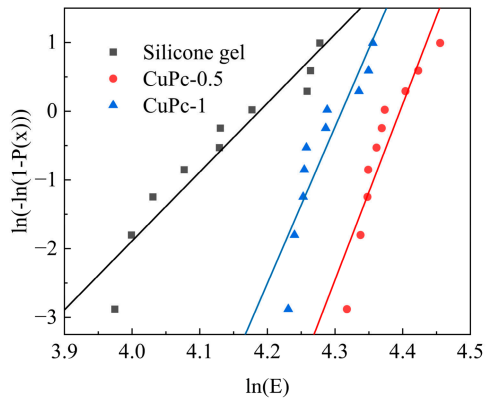


Figure 6. Measurement results of DC breakdown strength.

Table 1. The Weibull distribution fitting parameters.

Sample	β	E_0 (kV/mm)	95% CI of E_0 (kV/mm)
silicone gel	10	66	(62, 70)
CuPc-0.5	26	81	(79, 83)
CuPc-1	23	74	(72, 76)

Space charge can generate an additional electric field inside the material. When a large amount of charge accumulates locally, it distorts the original electric-field distribution and may create local high-field regions, thereby reducing the material's ability to withstand an externally applied DC voltage. The space charge and trap results discussed above show that the effect of CuPc on DC breakdown performance is closely related to its regulation of carrier transport. The relatively high space charge accumulation in silicone gel intensifies local electric-field distortion, resulting in the lowest DC breakdown field strength. CuPc-0.5 has the lowest residual space charge and simultaneously exhibits the highest DC breakdown field strength, indicating that an appropriate amount of CuPc can effectively reduce space charge accumulation and the associated electric-field distortion by altering the distribution of localized states and restricting long-range carrier migration. For CuPc-1, although the space charge remains substantially lower than that in silicone gel, the presence of lower-energy traps and more active detrapping-migration processes weakens this suppression, resulting in a lower DC breakdown field strength than that of CuPc-0.5.

2.5. Discussion of Charge Transport and Insulation Performance

The space charge, IRC, effective trap-energy distribution, and DC breakdown results provide complementary information on the electrical response of CuPc-modified silicone gel. The PEA measurements characterize the spatial distribution and persistence of net charge, whereas the IRC measurements describe the relaxation response following voltage removal. Analysis of these results together provides a basis for discussing how changes in trap-related charge dynamics are associated with reduced space charge accumulation and improved insulation performance. The discussion therefore focuses on charge accumulation, relaxation, and the resulting electric-field redistribution.

2.5.1. Effects of CuPc on Charge Trapping and Transport

CuPc is an organic semiconductor with a planar macrocyclic π-conjugated structure [24], as illustrated in Figure 7. Its electronic structure provides a physical basis for considering changes in localized electronic states when it is incorporated into silicone gel. Experimentally, CuPc addition modifies both the effective trap-energy distribution and the depolarization-current response. These changes support the involvement of trap-related processes in the altered electrical behavior of the composites.

Deep traps can contribute to the suppression of bulk space charge accumulation by influencing carrier transport and charge injection. Previous studies have shown that deep trapping states can capture charge carriers and restrict their penetration into polymer insulation, while interfacial deep traps can contribute to improved space charge and DC breakdown characteristics [25–27]. In particular, when injected carriers are trapped near the electrode, the resulting homocharge may generate an electric-field component opposing the injection field, thereby limiting further charge injection [25]. Consequently, fewer carriers may penetrate the specimen bulk and contribute to extended space charge accumulation. This mechanism is consistent with the reduced bulk charge densities and weaker charge penetration observed in the CuPc-containing specimens.

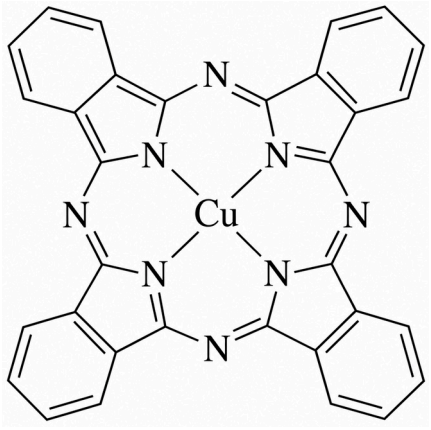


Figure 7. Molecular structure of CuPc.

The PEA results are consistent with this mechanism. During high-field polarization, silicone gel develops a broad charge-distribution region extending from the electrode vicinity into the specimen interior. In contrast, the CuPc-containing composites exhibit substantially weaker charge penetration and lower bulk charge densities. The difference is already apparent during voltage application, indicating that CuPc influences the establishment of space charge accumulation rather than merely accelerating charge dissipation after short circuit. At the beginning of the short circuit, the mean bulk charge densities of silicone gel, CuPc-0.5, and CuPc-1 are approximately 3.6, 1.1, and 1.3 C/m^3, respectively. After 1800 s, silicone gel retains approximately 2.5 C/m^3, whereas both composites exhibit values below 1 C/m^3. These observations support a reduction in charge accumulation within the bulk, consistent with trap-mediated restriction of carrier penetration and modification of the injection–transport–extraction balance.

The role of trap density must nevertheless be distinguished from that of trap occupation. The increased effective trap density indicates a greater contribution from trapping states within the adopted relaxation model, but it does not imply that all such states are occupied. The population of trapped carriers is determined by carrier supply and the competition among trapping, detrapping, and transport processes. Furthermore, the depth of a trap primarily determines the characteristic release time rather than the amount of accumulated charge. Thus, the increased contribution of deeper trapping states provides a plausible mechanism for restricting carrier transport, whereas the measured reduction in bulk space charge reflects the combined outcome of trapping and charge exchange at the electrodes.

The IRC results further clarify the influence of CuPc on charge relaxation. The initial relaxation currents increase from approximately 10 pA for silicone gel to 37 pA for CuPc-0.5 and 110 pA for CuPc-1, despite the lower residual bulk charge densities of the composites. This difference is attributable to the distinct quantities represented by the two measurements: PEA resolves the spatial distribution of net space charge, whereas IRC records the external current associated with charge motion and polarization relaxation. Consequently, a higher initial IRC does not necessarily indicate a greater amount of residual bulk charge.

The reconstructed trap spectra also reveal differences in the energy distribution of the relaxation response. Although both composites exhibit increased effective trap densities across the analyzed range, CuPc-1 has a more pronounced contribution in the relatively lower-energy region of approximately 0.78–0.87 eV. Within the thermally activated detrapping model, lower trap energies correspond to shorter characteristic release times under otherwise identical conditions. This feature is compatible with the stronger early-stage IRC response of CuPc-1. Meanwhile, CuPc-1 exhibits slightly greater residual bulk charge than CuPc-0.5, indicating that a stronger relaxation-current response does not necessarily

correspond to more effective suppression of space charge accumulation. The electrical behavior is therefore governed by the combined influence of trap availability, carrier residence time, and charge transport, rather than by the magnitude of the IRC or the effective trap density alone.

Overall, the PEA and IRC observations support a mechanism in which CuPc-modified trapping states influence both carrier penetration during polarization and charge relaxation after voltage removal. Deep-trap-assisted restriction of carrier transport, together with its possible influence on electrode injection, provides a physical explanation for the reduced bulk space charge. The contribution of individual injection, extraction, and relaxation processes cannot be uniquely separated from the present measurements, but their coupled influence is consistent with the observed spatial and temporal charge behavior.

2.5.2. Space-Charge-Induced Electric-Field Distortion and DC Breakdown Performance

The effect of space charge on insulation performance is ultimately reflected in the redistribution of the internal electric field. According to Poisson's equation,

$$\frac{dE(x)}{dx} = \frac{\rho(x)}{\varepsilon} \tag{2}$$

where $\rho(x)$ is the space charge density, and ε is the dielectric permittivity of the material. Therefore, the additional electric field generated by space charge can be approximately expressed as

$$\Delta E_{sc}(x) = \frac{1}{\varepsilon}\int \rho(x)dx \tag{3}$$

The actual local electric field can be written as

$$E_{loc}(x) = E_{app}(x) + \Delta E_{sc}(x) \tag{4}$$

When a large amount of space charge accumulates in a certain region, the local electric field deviates substantially from the average applied electric field, forming a local high-field region. Breakdown can occur once the maximum local electric field exceeds the critical local field strength corresponding to irreversible electrical damage of the material. Therefore, provided that the intrinsic material structure has not fundamentally changed, reducing the space charge density and the additional electric field is an important route to improving the macroscopic breakdown field strength. Figure 8 presents the spatiotemporal electric-field distributions reconstructed from the PEA measurements for silicone gel, CuPc-0.5, and CuPc-1, respectively, during stepwise DC polarization and subsequent short circuit.

The reconstructed electric-field distributions reveal a substantial difference between silicone gel and the CuPc-containing composites. At an applied average field of 15 kV/mm, the maximum local field in silicone gel approaches approximately 30 kV/mm, indicating pronounced space-charge-induced field enhancement. In contrast, the CuPc-containing composites exhibit substantially weaker field enhancement within the bulk. To further evaluate the influence of space charge on the internal electric-field distribution, the electric-field distortion rate was calculated as follows:

$$D(E_a, T) = \frac{E_m - E_a}{E_a} \times 100\% \tag{5}$$

where D is the electric-field distortion rate, E_m is the maximum electric-field strength within the specimen obtained from Poisson's equation, E_a is the externally applied average electric-field strength, and T is the measurement temperature.

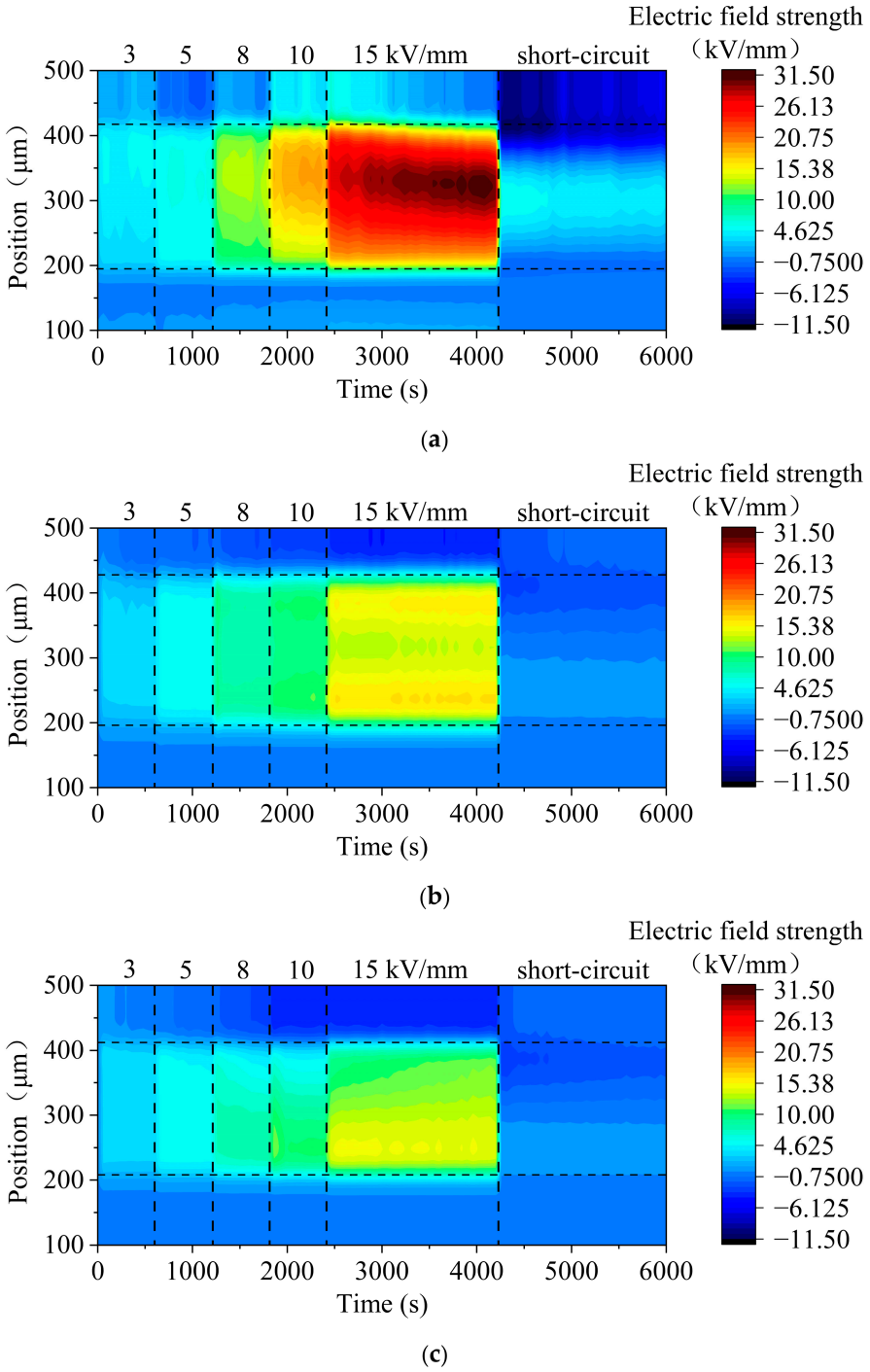


Figure 8. Electric-field distributions: (**a**) silicone gel; (**b**) CuPc-0.5; (**c**) CuPc-1.

Figure 9 compares the electric-field distortion rates of the three specimens under different applied electric fields. Silicone gel exhibits pronounced electric-field distortion, particularly under higher applied fields, whereas both CuPc-containing composites show substantially lower distortion levels. These results indicate that CuPc incorporation effectively mitigates space-charge-induced local electric-field enhancement, resulting in a more uniform internal electric-field distribution.

This result is consistent with the charge-transport behavior discussed in Section 2.5.1. When charge penetrates the bulk and accumulates nonuniformly, the resulting internal field can considerably exceed the externally applied average field in certain regions. Such local enhancement may further influence field-dependent carrier injection and transport,

potentially contributing to additional charge redistribution. By limiting the development of extended bulk charge distributions, CuPc reduces the associated local-field enhancement and the electrical stress imposed on the specimen interior. After voltage removal, the weaker residual fields in the composites are likewise consistent with their lower retained bulk charge densities.

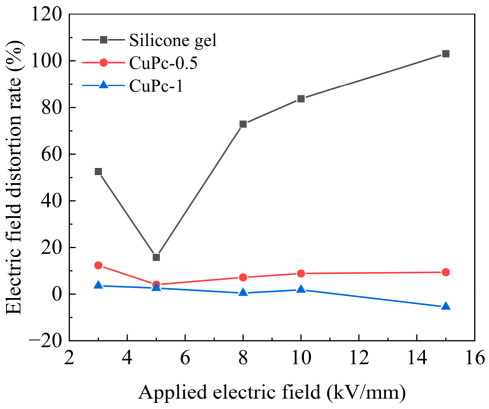


Figure 9. Distortion rates of silicone gel, CuPc-0.5, and CuPc-1.

The reduced local field enhancement provides an important physical basis for the improved DC breakdown performance. Regions subjected to elevated electrical stress are more susceptible to localized electrical failure, even when the average applied field is lower than the local field. The suppression of charge-induced field enhancement therefore helps alleviate the nonuniform electrical stress within the insulation. This interpretation is consistent with the improved DC breakdown performance, with the characteristic breakdown strengths of CuPc-0.5 and CuPc-1 increasing by approximately 23.1% and 13.0%, respectively, compared with silicone gel. The higher Weibull shape parameters of the composites also indicate reduced dispersion in the measured breakdown data.

Nevertheless, the reconstructed field distortion does not uniquely determine the breakdown-strength ranking. CuPc-1 exhibits lower reported distortion than CuPc-0.5 at certain applied fields, whereas CuPc-0.5 has the higher characteristic DC breakdown strength. This difference reflects the fact that the reconstructed electric fields characterize charge-induced stress under the PEA polarization conditions, while breakdown is also influenced by material heterogeneity, local defects, electrode configuration, and the applied voltage history. The field-reconstruction results therefore identify a significant contribution of space charge suppression to the improved DC breakdown performance, rather than establishing a direct proportional relationship between field distortion and breakdown strength.

The square-wave PDIV results provide a complementary assessment under rapidly varying electrical stress. The slightly higher mean PDIVs of the CuPc-containing composites indicate a modest change in discharge inception under the specified rod–plane configuration. Unlike DC breakdown, discharge inception under a 1 kHz unipolar square-wave with a rise time of 100 ns depends on the transient electric field associated with the dielectric response, as well as charge redistribution, electrode contact conditions, and possible gas-filled interfacial regions. Therefore, the DC space charge and field-reconstruction results should not be directly extended to square-wave PDIV. The relatively small change in PDIV, compared with the improvement in DC breakdown strength, reflects the different physical conditions governing these two insulation responses.

3. Conclusions

This study investigated the effects of CuPc on the space charge behavior, trap characteristics, and insulation performance of silicone gel, revealing a clear concentration-dependent regulation mechanism. The main conclusions are as follows:

1. CuPc incorporation effectively reduced bulk space charge accumulation during DC polarization and subsequent short-circuit depolarization. At the beginning of the short-circuit stage, the mean absolute bulk space charge densities of silicone gel, CuPc-0.5, and CuPc-1 were approximately 3.6, 1.1, and 1.3 C/m^3, respectively. After 1800 s of short circuit, the residual charge densities of both CuPc-containing composites decreased to below 1 C/m^3, compared with approximately 2.5 C/m^3 for silicone gel. Among the investigated specimens, CuPc-0.5 exhibited the strongest suppression of bulk space charge accumulation.
2. CuPc incorporation significantly modified the trap characteristics of silicone gel. The effective trap energy distributions reconstructed from IRC measurements showed that both CuPc-containing composites exhibited higher effective deep-trap densities than silicone gel. The increased contribution of deep trapping states is consistent with the suppression of bulk space charge accumulation, suggesting that changes in trapping characteristics contribute to the regulation of charge transport within the material.
3. The internal electric-field distributions demonstrated that CuPc incorporation substantially mitigated space-charge-induced electric-field distortion. At an applied field of 15 kV/mm, the maximum local field in silicone gel approached 30 kV/mm, and its electric-field distortion rate reached approximately 103%. Both CuPc-containing composites exhibited weaker local electric-field enhancement and more uniform field distributions, consistent with their reduced bulk space charge accumulation.
4. CuPc significantly improves DC breakdown performance while slightly increasing PDIV. CuPc addition improved the characteristic DC breakdown strength from approximately 66 kV/mm for silicone gel to 81 and 74 kV/mm for CuPc-0.5 and CuPc-1, respectively. Among the investigated compositions, CuPc-0.5 exhibited the highest characteristic breakdown strength. The present results provide initial evidence of the potential of CuPc modification for improving DC insulation performance.

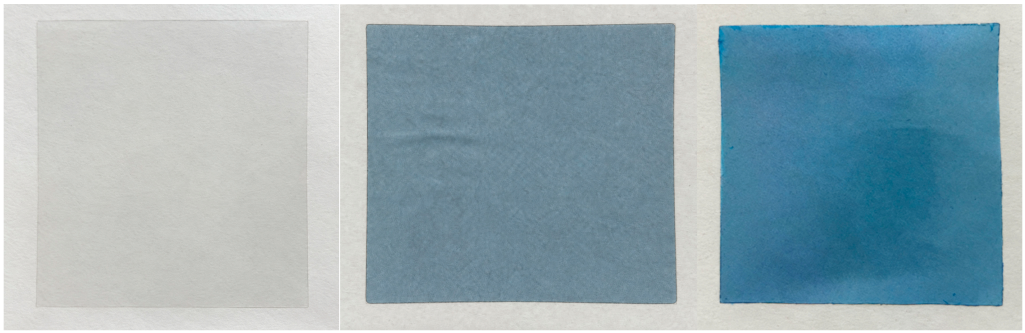
4. Materials and Methods

4.1. Preparation of CuPc-Doped Composite Specimens

The silicone gel used in this study was Ausbond-195T, a two-component silicone potting compound purchased from Shenzhen Ausbond Co., Ltd. (Shenzhen, China). Copper phthalocyanine (β type) was purchased from Shanghai Macklin Biochemical Technology Co., Ltd. (Shanghai, China). The filler was in powder form and had a nominal particle size of 2 μm. Three specimens were prepared: silicone gel, silicone gel doped with 0.5 wt.% CuPc, and silicone gel doped with 1 wt.% CuPc. These samples are denoted as silicone gel, CuPc-0.5, and CuPc-1, respectively. The three specimen types are shown in Figure 10.

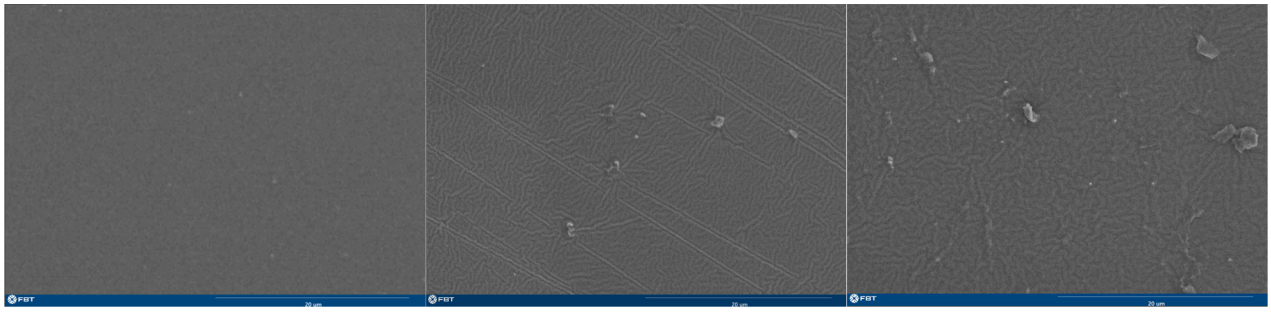
Scanning electron microscopy (SEM) was used to examine the surface morphology of the silicone gel and the dispersion state of CuPc in the cured composites, as presented in Figure 11. The SEM images in Figure 11a–c show the silicone gel, CuPc-0.5, and CuPc-1, respectively. The silicone gel exhibits a relatively smooth and uniform surface without obvious particle-like features. After the incorporation of 0.5 wt.% CuPc, a few scattered bright particle-like features can be observed on the specimen surface, as shown in Figure 11b. When the CuPc content increases to 1 wt.%, more irregular bright features become visible, as shown in Figure 11c. Overall, the observations suggest relatively good filler dispersion in the examined surface regions, although some localized aggregation may occur at the

higher CuPc concentration. During preparation, CuPc was weighed according to the specified mass fraction and added to component A of the silicone compound, followed by mechanical stirring at 500 rpm for 20 min to promote uniform dispersion of CuPc in the matrix. Component B was then added at an A:B mass ratio of 10:1, and the mixture was mechanically stirred at 500 rpm for an additional 2 min. The mixed compound was placed in a vacuum oven and degassed for 20 min to remove bubbles introduced during stirring. After degassing, the compound was slowly poured into a mold and placed in a flat-plate vulcanizing press, where it was cured for 24 h at room temperature under a pressure of 15 MPa, yielding film samples with a thickness of approximately 200 μm. All three specimen groups were prepared using identical stirring, degassing, molding, and curing conditions, with the CuPc content being the only intentionally varied compositional parameter.



(**a**) (**b**) (**c**)

Figure 10. Samples: (**a**) silicone gel; (**b**) CuPc-0.5; (**c**) CuPc-1.



(**a**) (**b**) (**c**)

Figure 11. Scanning electron microscopy: (**a**) silicone gel; (**b**) CuPc-0.5; (**c**) CuPc-1.

4.2. Partial Discharge Measurement

To suppress switching interference associated with the high dV/dt of the square-wave voltage while reducing the requirements imposed by high-frequency partial discharge (PD) signals on the sampling rate and data-storage capacity of the acquisition system, a down-mixing system was employed for PD detection. The circuit diagram and photo of the down-mixing PD detection system are shown in Figure 12. The PD signal received by the antenna was first filtered and amplified and then fed into a mixer together with a fixed-frequency local oscillator (LO) signal. The received signal passes through a frequency-selective RF filter to suppress out-of-band switching interference and is then amplified by the RF front-end amplifier. The conditioned signal is applied to the RF port of the mixer, while a stable local-oscillator signal is fed to its LO port. At the mixer output, an intermediate-frequency (IF) filter suppresses the sum-frequency component and unwanted mixing products, and the retained difference-frequency signal is amplified and delivered to the data-acquisition instrument for PD identification. In this manner, the characteristic

information of the PD signal could be preserved while substantially reducing the bandwidth requirements of the downstream data-acquisition and signal-processing system [28]. The PD testing system is shown in Figure 13.

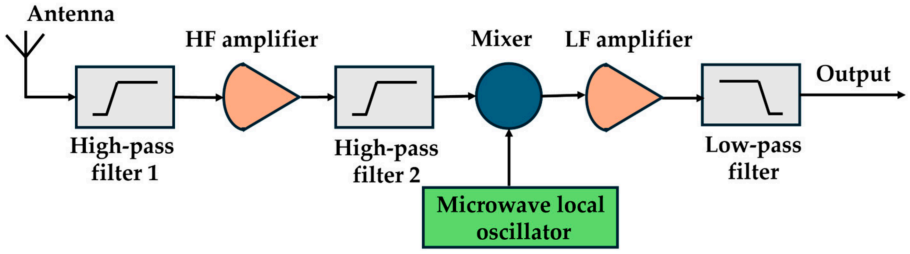


Figure 12. Circuit diagram of the down-mixing PD detection system.

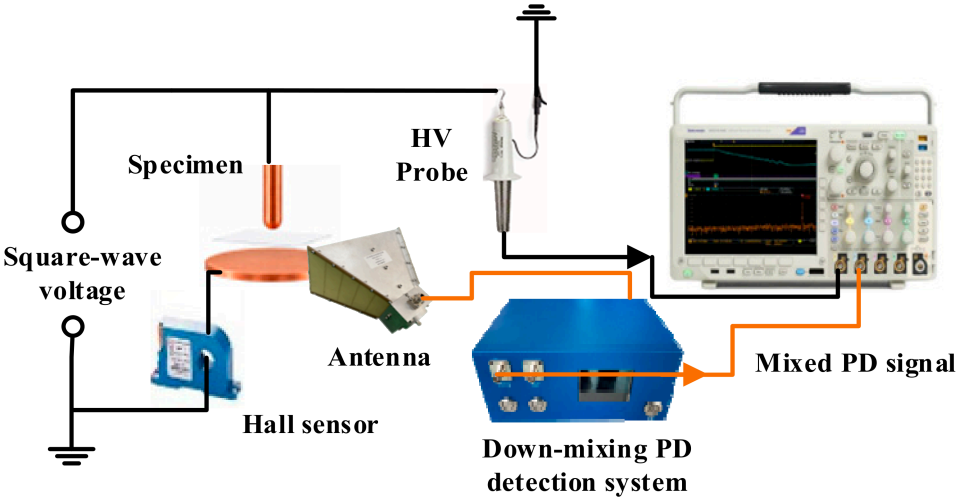


Figure 13. PD testing system.

For the PD measurement, the specimen was placed between a rod electrode and a plane electrode. The tip radius was 0.5 mm, and the plane-electrode diameter was 25 mm. The rod electrode was in direct contact with the specimen. Identical electrode geometry, contact conditions, and environmental conditions were maintained for all compositions. A unipolar high-voltage square-wave source with a frequency of 1 kHz and a rise time of 100 ns was used as the excitation source. The applied voltage was continuously increased at a rate of 100 V/s until repetitive PD signals were detected. Ten independent measurements were performed for each material group. The aperture of an ultra-high-frequency (UHF) horn antenna was directed toward the PD region and positioned approximately 10 cm away from the discharge site to enable non-contact detection of the high-frequency electromagnetic radiation generated by PD events [29]. The voltage applied to the specimen was monitored online using a high-voltage probe. Meanwhile, the circuit current was measured using a Hall-effect current sensor. When the average current flowing through the specimen exceeded 0.5 A, the square-wave source automatically ceased its output to provide overcurrent protection.

To distinguish PD signals from switching-induced electromagnetic interference (EMI) under unipolar square-wave excitation, frequency-selective filtering and down-mixing were employed to suppress the interference associated with voltage transitions [29]. In the processed time-domain waveform, commutation EMI was characterized by the transient response accompanying the switching edge, whereas PD was identified by distinct impulsive signals that could be clearly distinguished from the residual interference in terms of

waveform characteristics and amplitude. As illustrated in Figure 14, the detected PD pulse can be distinguished from the switching-related EMI. During the voltage ramp, the peak value of the applied square-wave voltage at which identifiable PD pulses were repeatedly detected was recorded as the PDIV.

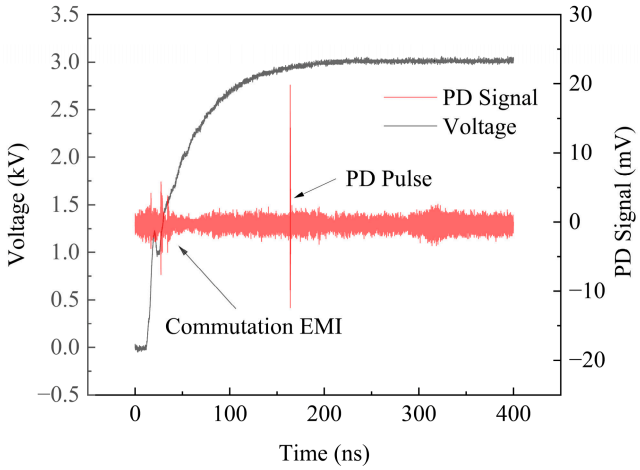


Figure 14. Typical voltage and PD waveforms.

4.3. Space Charge and IRC Measurements

The PEA method was employed to characterize the spatial distribution of space charge within the specimens. In this method, a nanosecond voltage pulse interacts with the charges in the specimen to generate acoustic waves, which are detected by a piezoelectric sensor and converted into electrical signals to reconstruct the space charge distribution. IRC measurements were used to investigate the charge relaxation behavior after removal of the applied DC voltage. During polarization, charge carriers may be injected from the electrodes and trapped within the material, while dipolar and interfacial polarization can also be established. After removal of the applied voltage, trapped carriers may be released and transported, while the previously established polarization gradually relaxes, giving rise to a time-dependent current in the external circuit. This current is recorded as the IRC, which provides information on charge relaxation and can be further analyzed to estimate the effective trap energy distribution.

A combined space charge and current measurement system was employed to investigate the space charge distributions and current responses of silicone gel specimens with different CuPc contents. During the same experimental procedure, the space charge within the specimen and the current flowing through the specimen were jointly monitored, enabling characterization of space charge accumulation, migration, and decay under different electric fields, together with the corresponding charge-carrier transport behavior [30].

During the measurements, the specimen was placed between the upper and lower electrodes of a PEA measurement system, and DC electric fields of 3, 5, 8, 10, and 15 kV/mm were sequentially applied. The electric-field application time at 3, 5, 8, and 10 kV/mm was 600 s for each electric-field level, whereas polarization at 15 kV/mm was maintained for 1800 s. After completion of the polarization process at 15 kV/mm, the applied electric field was removed, and the two electrodes of the specimen were short-circuited. Measurements were then continued for an additional 1800 s to characterize the dissipation of residual space charge within the specimen after voltage removal, as well as the decay behavior of the depolarization current.

To prevent the nanosecond pulse voltage required for PEA measurements from interfering with the measurement of weak currents, the space charge and current signals

were measured using a time-interleaved measurement scheme [30]. During space charge measurement, the nanosecond pulse-voltage source was activated, and the single-pole double-throw (SPDT) switch was connected to the grounding terminal. The acoustic signal generated by the nanosecond pulse excitation was converted by a piezoelectric sensor and subsequently transmitted to an oscilloscope through a broadband amplifier, thereby allowing the space charge distribution within the specimen to be obtained. During current measurement, the output of the nanosecond pulse-voltage source was temporarily suspended, and the SPDT switch was connected to the current-meter terminal. This configuration enabled the weak current flowing through the specimen to be fully acquired without interference from the pulse voltage.

During each DC voltage application stage and the subsequent short-circuit stage after voltage removal, the current and space charge signals were periodically acquired in an alternating manner according to the procedure described above. Each current measurement and each space charge measurement lasted for 30 s, resulting in a complete combined measurement cycle of 60 s. Within each cycle, the current was measured first, followed by the space charge measurement. In this way, the current response and space charge distribution of the specimen could be obtained under essentially identical electric-field and temporal conditions. The overall simultaneous measurement system is shown in Figure 15.

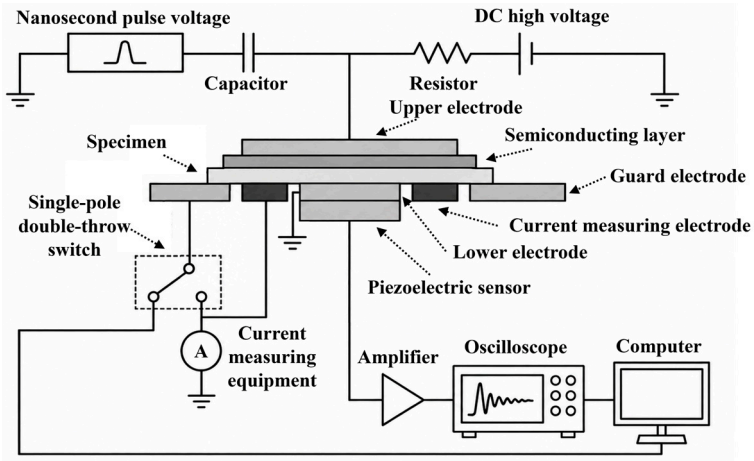


Figure 15. PEA and IRC measurement system.

The PEA and IRC measurements were repeated five times for each specimen composition under identical experimental conditions. The relative variation in the mean absolute bulk space charge density at the end of the 15 kV/mm DC polarization stage was within 10% among the repeated measurements, indicating good experimental repeatability. Therefore, representative space charge distributions and IRC decay curves were selected for presentation.

4.4. Calculation of Trap Characteristics

The effective initial occupied-trap energy distribution was reconstructed from IRC using the first-order detrapping and non-negative least-squares framework of Zhao et al. [31]. The analysis used a constant temperature of 293 K. Carrier transit after release was assumed to be fast relative to detrapping, with retrapping omitted from the inversion kernel. Here, $t = 0$ denotes the start of depolarization.

For a trap with energy depth E, the detrapping rate $D(E)$ is

$$D(E) = sexp\left(-\frac{E}{k_B T}\right) \quad (6)$$

The characteristic detrapping time $\tau(\mathrm{E})$ is

$$\tau(E) = \frac{1}{D(E)} \tag{7}$$

where s is the effective attempt-to-escape frequency and is set at 4.17×10^{13} s^{-1} in this paper based on the theoretical modeling of the infinitely deep square potential well as described in [32]. k_B is the Boltzmann constant, and $\tau(\mathrm{E})$ is the characteristic detrapping time.

Let $N_t(E)$ denote the density of available trap states per unit volume and unit energy, and let $f_0(E)$ denote their occupancy probability at the beginning of depolarization. The effective initial occupied-trap distribution is then defined as

$$N_{occ}(E) = f_0(E)N_t(E) \tag{8}$$

Let $n(E, t)$ denote the density of traps that remain occupied at energy depth E and time t during depolarization, expressed per unit volume and unit energy. Under the first-order detrapping model, the rate of decrease in this density is proportional to the remaining occupied-trap density:

$$\frac{\partial n(E,t)}{\partial t} = -D(E)n(E,t) \tag{9}$$

At the beginning of depolarization, the occupied-trap density is given by the initial distribution:

$$n(E,0) = N_{occ}(E) \tag{10}$$

Solving the rate equation with this initial condition gives

$$n(E,t) = N_{occ}(E)\exp[-D(E)t] \tag{11}$$

which describes the exponential decay of the occupied-trap population at each energy depth during depolarization.

The release rate over an energy interval dE is $D(E)\ N_{occ}\ (E)\exp[-D(E)t]dE$, giving the response kernel

$$G(E,t) = D(E)\exp[-D(E)t] \tag{12}$$

Under the planar-electrode approximation in [31], the effective occupied-trap population is taken as uniform through the specimen thickness L. Integration over trap energy yields

$$J(t) = \frac{qL}{2}\int_{E_{\min}}^{E_{\max}} G(E,t)N_{occ}(E)dE \tag{13}$$

The measured relaxation current is

$$I(t) = I_b + SJ(t) \tag{14}$$

where q is the elementary charge, S is the electrode area, and I_b is the background current.

The interval $E_{min} = 0$ eV to $E_{max} = 2$ eV was discretized into $M = 200$ equally spaced energy points ($dE = 0.01$ eV). At measurement times t_i, the background-corrected current density is defined as

$$J_i = \frac{I(t_i) - I_b}{S} \approx \sum_{j=1}^{M} G_{ij}N_j \tag{15}$$

where $N_j = N_{occ}(E_j)$ is the unknown effective initial occupied-trap density per unit energy at E_j. The coefficient G_{ij} describes the contribution of a unit occupied-trap spectral density at E_j to the current density at t_i, including the energy-integration weight:

$$G_{ij} = \frac{qL}{2}D\left(E_j\right)\exp\left[-D\left(E_j\right)t_i\right]\Delta E \tag{16}$$

The vector $J = [J_1, \ldots, J_m]^T$ contains the background-corrected measured current densities, and $N = [N_1, \ldots, N_m]^T$ contains the unknown occupied-trap spectral densities. Each column of G describes the current response at one energy point. Here, m is the number of measurement times. The distribution is obtained by solving

$$\begin{cases} J \approx GN \\ \hat{N} = \underset{N \geq 0}{\operatorname{argmin}} \|GN - J\|_2^2 \end{cases} \tag{17}$$

The non-negativity constraint ensures physically admissible occupied-trap densities. The fitted values $\hat{N}$, plotted against their corresponding energies, give the reconstructed trap spectrum. Substitution into the forward model yields $\hat{J} = G\hat{N}$ and $\hat{I}(t_i) = I_b + S\hat{J}_i$. The reconstructed IRC curve agreed with the measured data, with $R^2 = 0.997$.

All compositions were analyzed using the same temperature, attempt-to-escape frequency, and energy grid. The recovered spectrum reflects both trap availability and initial occupancy under the specified polarization conditions. The reported R^2 assesses current reconstruction rather than establishing the uniqueness of the recovered spectrum.

4.5. Breakdown Test

The DC breakdown performance of silicone gel specimens with different CuPc contents was tested using a sphere–plane electrode configuration. Both the spherical electrode and the plane electrode had a diameter of 25 mm. During the test, the specimen was placed between the two electrodes, and the applied voltage was continuously increased at a rate of 100 V/s until breakdown occurred. Ten independent specimens were tested for each material group.

Considering the statistical nature of dielectric breakdown, the measured DC breakdown strengths were analyzed using a two-parameter Weibull distribution:

$$P_f = 1 - \exp\left[-\left(\frac{E}{E_0}\right)^{\beta}\right] \tag{18}$$

where P_f is the cumulative breakdown probability, E is the measured breakdown field strength, E_0 is the characteristic breakdown strength corresponding to $P_f = 63.2\%$, and β is the Weibull shape parameter reflecting the dispersion of the breakdown data. The equation can be linearized as

$$\ln\left[-\ln\left(1 - P_f\right)\right] = \beta lnE - \beta \ln E_0 \tag{19}$$

For the ten breakdown measurements in each group, the data were arranged in ascending order, and the cumulative breakdown probability was calculated according to

$$P_{f,i} = \frac{i - 0.5}{n + 0.25} \tag{20}$$

where i is the rank of the measured breakdown strength, and n is the total number of specimens.

For each composition, ten independent breakdown measurements were analyzed using a two-parameter Weibull distribution. The characteristic breakdown strength E_0 and shape parameter β were estimated by maximum likelihood. Approximate 95% confidence intervals for E_0 were calculated using the log-transformed Wald method as

$$E_{0,L} = \exp\left[\ln \hat{E}_0 - 1.96\mathrm{SE}\left(\ln \hat{E}_0\right)\right] \tag{21}$$

$$E_{0,U} = \exp\left[\ln \hat{E}_0 + 1.96\mathrm{SE}\left(\ln \hat{E}_0\right)\right] \tag{22}$$

where $\hat{E}_0$ is the estimated characteristic breakdown strength. The standard error was obtained from the inverse observed information matrix evaluated at the maximum-likelihood

estimates. The resulting confidence limits quantify the statistical uncertainty in the estimated E_0.

Author Contributions: Conceptualization, K.C. and Y.W.; methodology, K.C. and Y.W.; formal analysis, K.C. and C.X.; resources, Y.W. and C.X.; writing—original draft preparation, C.X. and K.C.; writing—review and editing, K.C., Y.W. and C.X.; project administration, Y.W.; funding acquisition, Y.W. All authors have read and agreed to the published version of the manuscript.

Funding: This research was funded by the Open Fund of the State Key Laboratory of Advanced Power Transmission Technology (Project: Research on Methods for Improving the Electro-Thermal Reliability of High-Overcurrent-Capability Power Semiconductor Device Packaging; grant number: SGDK0000DLQT2507103).

Institutional Review Board Statement: Not applicable.

Informed Consent Statement: Not applicable.

Data Availability Statement: The data presented in this study are openly available in the article.

Conflicts of Interest: Author Chao Xiao was employed by the company China Electric Power Research Institute Co., Ltd. The remaining authors declare that the research was conducted in the absence of any commercial or financial relationships that could be construed as a potential conflict of interest.

References

1. Ali, M.A.; Jiang, X.; Gadow, S.I.; Deusdedith, R.W. Enhancing hydrophobic stability of silicone rubber insulators under high-voltage direct current stress through optimised nano-fumed silica surface area: A dynamic drop test study. *High Volt.* **2026**, *11*, 823–837. [CrossRef]
2. Chen, K.; Gao, T.; Xu, M.; Zhan, Y.; Hou, S.; Fu, M.; Liao, Y.; Lin, M. Study on the aggregation structure and DC conductivity and breakdown characteristics of polypropylene insulation for HVDC cables. *High Volt.* **2025**, *10*, 1451–1463. [CrossRef]
3. Wang, Y.; Xu, R.; Ren, P.; Wang, Y.; Chen, H.; Wu, W.; Yang, X. Effects of heavy load temperature rise on the dynamic charge transport characteristics of XLPE/SiR heterogeneous insulation. *High Volt.* **2025**, *10*, 964–975. [CrossRef]
4. Zhan, A.; Ye, F.; Tian, S.; Zhang, G.; Zhang, X. Combustion characteristics and self-extinguishing mechanism of novel self-extinguishing fluorinated silicone insulating oil. *High Volt.* **2025**, *10*, 1144–1153. [CrossRef]
5. He, D.; Wang, H.; Li, Y.; Wang, Y.; Li, Q.; Li, Q. The temperature and voltage resistance performance of phenyl-modified silicone elastomers for high-voltage and high-power semiconductor device encapsulation. *High Volt.* **2025**, *10*, 1135–1143. [CrossRef]
6. Yuan, C.; Xie, C.; Li, L.; Xu, X.; Gubanski, S.M. Surface potential decay on material samples taken from in-service aged HVDC silicone rubber composite insulators. *IEEE Trans. Dielectr. Electr. Insul.* **2017**, *24*, 592–600. [CrossRef]
7. Yuan, C.; Xie, C.; Li, L.; Xu, X.; Gubanski, S.M.; Zhou, Y.; Li, Q.; He, J. Space charge behavior in silicone rubber from in-service aged HVDC composite insulators. *IEEE Trans. Dielectr. Electr. Insul.* **2019**, *26*, 843–850. [CrossRef]
8. Wang, X.; Chen, C.; Xiong, J.Z.; Wu, K.; Tu, D.M. Formation mechanism of space charge in silicone rubber insulation under low DC stress. In Proceedings of the 2015 IEEE 11th International Conference on the Properties and Applications of Dielectric Materials (ICPADM), Sydney, Australia, 19–22 July 2015; pp. 116–119. [CrossRef]
9. Hussain, R.; Moxter, J.; Hinrichsen, V. Influence of temperature and electric field strength on the space charge behavior of liquid silicone rubber with carbon black nanofillers. *IEEE Trans. Dielectr. Electr. Insul.* **2020**, *27*, 427–432. [CrossRef]
10. Zhou, T.; Chen, G.; Liao, R.; Xu, Z. Charge trapping and detrapping in polymeric materials: Trapping parameters. *J. Appl. Phys.* **2011**, *110*, 043724. [CrossRef]
11. Li, J.; Zhou, F.; Min, D.; Li, S.; Xia, R. The energy distribution of trapped charges in polymers based on isothermal surface potential decay model. *IEEE Trans. Dielectr. Electr. Insul.* **2015**, *22*, 1723–1732. [CrossRef]
12. Zhang, C.; Lv, Z.; Xu, Z.; Wu, K.; Morshuis, P.; Claverie, A. Space charge in PDMS/SiO_2 nanocomposites under DC voltage and its influence on breakdown properties. *IEEE Trans. Dielectr. Electr. Insul.* **2024**, *31*, 947–955. [CrossRef]
13. Du, B.X.; Li, Z.L.; Yang, Z.R. Field-dependent conductivity and space charge behavior of silicone rubber/SiC composites. *IEEE Trans. Dielectr. Electr. Insul.* **2016**, *23*, 3108–3116. [CrossRef]
14. Li, Z.L.; Du, B.X.; Yang, Z.R.; Li, J. Effects of crystal morphology on space charge transportation and dissipation of SiC/silicone rubber composites. *IEEE Trans. Dielectr. Electr. Insul.* **2017**, *24*, 2616–2625. [CrossRef]
15. Du, B.X.; Yang, Z.R.; Li, Z.L.; Li, J. Temperature-dependent nonlinear conductivity and carrier mobility of silicone rubber/SiC composites. *IEEE Trans. Dielectr. Electr. Insul.* **2018**, *25*, 1080–1087. [CrossRef]

16. Du, B.X.; Yang, Z.R.; Li, Z.L.; Li, J. Nonlinear conductivity and charge transport characteristics of silicone rubber/SiC composites under impulse superimposed on DC voltage. *IEEE Trans. Dielectr. Electr. Insul.* **2019**, *26*, 776–783. [CrossRef]
17. Li, Z.; Yang, Z.; Du, B. Surface charge transport characteristics of ZnO/silicone rubber composites under impulse superimposed on DC voltage. *IEEE Access* **2019**, *7*, 3008–3017. [CrossRef]
18. Wang, F.; Hu, D.; Zhong, L.; Chen, S.; Wang, L. Surface charge dissipation characteristics of Al_2O_3/silicone rubber composites with different weight percentages. *IEEE Access* **2024**, *12*, 33337–33346. [CrossRef]
19. Reisz, B.; Belova, V.; Duva, G.; Zeiser, C.; Hodas, M.; Hagara, J.; Šiffalovič, P.; Pithan, L.; Hosokai, T.; Hinderhofer, A.; et al. Polymorphism and structure formation in copper phthalocyanine thin films. *J. Appl. Crystallogr.* **2021**, *54*, 203–210. [CrossRef] [PubMed]
20. Hu, J.; Chu, B.; Liu, X.; Wei, H.; Wang, J.; Kan, X.; Xia, Y.; Huang, S.; Chen, Y. Preparation of PANI/CuPc/PDMS composite elastomer with high dielectric constant and low modulus assisted by electric fields. *Polymers* **2024**, *16*, 1549. [CrossRef] [PubMed]
21. Huang, T.; Yuan, B.; Tang, J.; Zhang, Y. Enhanced electromechanical performance through chemistry graft copper phthalocyanine to siloxane-modified polyurethane and interpenetrate with siloxane silicon rubber as composite actuator material. *IET Nanodielectr.* **2021**, *4*, 38–44. [CrossRef]
22. Shimoga, G.; Shin, E.-J.; Lee, S.-H.; Devendrachari, M.C.; Choi, D.-S.; Kim, S.-Y. Electret gel interfaces of phthalo blue and plasticized PVC for enhanced vibrotactile actuation. *Sens. Actuators A Phys.* **2026**, *398*, 117357. [CrossRef]
23. Cantera Cantera, L.A.; Sánchez Vergara, M.E.; Hamui, L.; Mejía Prado, I.; Flores Huerta, A.; Martínez Plata, T.L. Analysis of a flexible photoconductor, manufactured with organic semiconductor films. *Micromachines* **2024**, *15*, 446. [CrossRef] [PubMed]
24. Rani, V.; Sharma, A.; Kumar, P.; Singh, B.; Ghosh, S. Charge transport mechanism in copper phthalocyanine thin films with and without traps. *RSC Adv.* **2017**, *7*, 54911–54919. [CrossRef]
25. Li, J.; Han, C.; Du, B.; Takada, T. Deep trap sites suppressing space charge injection in polycyclic aromatic compounds doped XLPE composite. *IET Nanodielectr.* **2020**, *3*, 10–13. [CrossRef]
26. Zhou, Y.; Zhu, Y.; Yuan, C.; Li, Q.; Xu, X.; Serdyuk, Y.; Wang, Q.; He, J. Enabling high-performance polypropylene nanocomposites with interfacial deep traps. *IEEE Trans. Dielectr. Electr. Insul.* **2023**, *30*, 484–487. [CrossRef]
27. Li, S.; Xie, D.; Lei, Q. Understanding insulation failure of nanodielectrics: Tailoring carrier energy. *High Volt.* **2020**, *5*, 643–649. [CrossRef]
28. Ding, Y.; Wang, Y.; Sun, H.; Yin, Y. High-temperature partial discharge characteristics of power module packaging insulation under square pulse with high dV/dt based on down-mixing method. *IEEE Trans. Ind. Electron.* **2023**, *70*, 7334–7342. [CrossRef]
29. Tenbohlen, S.; Denissov, D.; Hoek, S.M.; Markalous, S.M. Partial discharge measurement in the ultra high frequency (UHF) range. *IEEE Trans. Dielectr. Electr. Insul.* **2008**, *15*, 1544–1552. [CrossRef]
30. Wang, Y.; Wu, J.; Yin, Y. Relationship between space charge behavior and trap energy density distribution: A simultaneous measurement. *IEEE Trans. Dielectr. Electr. Insul.* **2019**, *26*, 738–745. [CrossRef]
31. Zhao, J.; He, R.; Gao, S.; Xiang, C.; Wang, Y.; Yin, Y. Study on charge transport and trap characteristics of silicone for power module encapsulation. *Insul. Mater.* **2022**, *55*, 64–71. (In Chinese) [CrossRef]
32. Atkins, P.W. *Physical Chemistry*, 4th ed.; Oxford University Press: Oxford, UK, 1990.

Disclaimer/Publisher's Note: The statements, opinions and data contained in all publications are solely those of the individual author(s) and contributor(s) and not of MDPI and/or the editor(s). MDPI and/or the editor(s) disclaim responsibility for any injury to people or property resulting from any ideas, methods, instructions or products referred to in the content.